A Generalized Low-Rank Double-Tensor Nuclear Norm Completion Framework for Infrared Small Target Detection

Lizhen Deng, *Member, IEEE,* Dongyuan Xu, Guoxia Xu, *Member, IEEE,* Hu Zhu, *Member, IEEE,*

Abstract—Infrared small target detection is a research hotspot in computer vision technology that plays an important role in infrared early warning systems. Specifically, infrared images with strong background clutter and noise pose a challenge to target detection technology. In this paper, we propose a method for infrared small target detection based on the double nuclear norm and ring structural elements over a generalized tensor framework. We use the double nuclear norm instead of the traditional single nuclear norm as the relaxation of the rank function, which solves the problem that the suboptimal solution deviates from the original solution and better approaches the rank minimization. In addition, we use weighted ring structural elements instead of traditional structural elements to make better use of the target information and its surrounding background. Experiments on six sequences of real images show that the proposed method can enhance the target and suppress the background effectively and ensure a high detection probability and a low false alarm rate.

Index Terms—Multi-frame infrared image, small target detection, double nuclear norm, ring Top-Hat regularization.

I. INTRODUCTION

INFRARED small target detection plays a critical role in signal processing and is widely used in many fields such as remote sensing [1], [2], medical imaging [3], target detection and tracking [4], and aerospace technology [5]. However, in a complex background environment, infrared targets have their own characteristics, making detection very difficult. First, the target imaging distance is generally far, and the target occupies only a few pixels in the image. Second, the noise and background clutter interference in the imaging system are strong, making the target signal relatively weak and easily submerged by a strong noise background. Finally, because the target lacks effective shape and texture features, there is little information that can be provided to the detection and tracking system. Currently, with the development of the tensor completion [6] [7] [8], top-hat filter [5], and matrix operations [9], more and more researchers are paying attention to the problem of infrared small target detection, which remains a challenging problem.

Since mathematical morphology was proposed by Matheron [18] and Serra [19], it has become an important tool for solving image processing problems. Mathematical morphology is a powerful non-linear image processing framework that provides useful tools for many tasks. It can be used to remove unnecessary parts [20] in an image, to segment the useful parts of an image [21], or to perform interpolation to fill in missing parts [22]. Morphological theory has recently been applied to the detection of small targets in infrared images. Specifically, the top-hat transform is widely used in image segmentation [24], [25], target detection [5], [23], image enhancement [26], [27], etc. These applications can be regarded as the application of the top-hat transform in point extraction. [28] proposed a detection method for small targets based on the top-hat transform, but because the infrared target is small, the image contains, the target has no obvious features, and the performance of speckle extraction is not ideal. If the SNR of the image is large, the top-hat transform can be applied to small target detection directly [23], the infrared target easily becomes submerged in the background with low SNR. [31], [32] proposed a method to enhance dim targets and suppress noise by introducing target attributes. However, this method needs prior knowledge, and the suppression effect is not obvious for bright interference. [35], [36] introduced two different structural elements for infrared small target detection. They constructed a circular structure factor to apply the difference information between the target region and the surrounding background directly to the structure elements, which yielded better detection results than the traditional top-hat transform. However, applying the top-hat transform alone is limited to enhancing the target and suppressing the background. The transform is not ideal for images with considerable clutter and blurred boundaries. In [33], the suspicious target region was extracted by a top-hat filter, and the effective local contrast measure was defined. They introduced their approach to the local self similarity calculation to determine the target. This method can accurately extract the target, but the background suppression effect remains limited [30] [29].

In infrared images, most of the area is occupied by the background, while the target occupies only a few pixels. Moreover, the local background and its adjacent area have strong correlation, and the target is sparse. In other words, the background is low rank and the target is sparse. Therefore, recovery of the low-rank matrix can be used to segment the target from the background. Low-rank matrix restoration has a wide range of applications in image restoration, signal

processing, computer vision, image processing, artificial intelligence and machine learning and promotes the development of signal sparse representation in compressed sensing. In the low-rank matrix recovery model, the problem of minimum rank optimization must be solved, but because the matrix rank is a non-convex discontinuous function, an NP problem is encountered. To solve this problem, we typically use the kernel norm [5] to replace the rank function because compared with the L_1 and L_2 norms, the structure error representation criterion based on the kernel norm is more effective. [37] constructed local patches to transform the traditional infrared small target detection problem into a low-rank sparse matrix recovery problem. [38] proposed an infrared patch tensor model based on the weighted tensor kernel norm, which uses the tensor kernel norm to recover the background and target. [39] extended the high-dimensional data clustering method based on non-Euclidean geometry to the traditional LRR method based on Grassmann manifold and achieved good performance. However, the low-rank subproblem based on the traditional kernel specification tends to over-express the rank components in the expression matrix, and when choosing low-rank constraints, these methods all use the traditional kernel specification, which will lead to the final result not being optimal but suboptimal [40], [41]. Therefore, some researchers use non-convex relaxation as a low-rank constraint to obtain a better solution. [42] used the Schatten-p norm of the non-convex rank relaxation function to recover the low-rank matrix. This approach achieved accurate solutions under the condition of only a weakly limiting isometric property. However, both the Schatten-p norm and kernel norm involve singular value decomposition of large-scale matrices to solve low-rank problems, which leads to considerable computational complexity when solving large-scale problems. In addition, the singular value components have different meanings, and the Schatten-p norm does not make a differentiated selection based on their importance. [43] proposed a double nuclear norm-based low-rank model on the Grassmann manifold (G-DNLR); they decomposed the matrix into a product of two low-rank matrices and used the decomposition matrix constraint to represent the double nuclear norm for the original matrix.The G-DNLR successfully exploited the local geometrical structure of the data space. Therefore, the double nuclear norm could effectively standardize the different low-rank components of tensor data and reduce the computational complexity,and solve the problem of background images.

Most of the above methods are implemented based on matrix factorization. In addition to it, some scholars have proposed methods based on tensor decomposition to solve low-rank models. Here we also do some introduction.It is not easy to directly extend from a matrix to a tensor, because there does not seem to be a unique definition of the rank of a tensor. The more commonly used definition are the CANDECOMP/PARAFAC (CP)-rank [48] [49] and the Tucker- rank [50] [51] (or denoted as "n-rank" in [52]). The CP-rank is based on the CP decomposition, while the Tucker rank is based on the Tucker decomposition. Braman et al. [53] and Kilmer et al. [54] proposed tensor singular value decomposition (t-SVD) on the basis of tensor-tensor product (t-prod). The overall operation avoids the distortion of tensor matrixization.Jiang et al. [55] summarized the tensor singular value decomposition (t-SVD) and proposed tensor multi-rank and the tensor tubal-rank. Recently, Based on the CP decomposition of tensors, Xue et al. [56] proposed a new tensor decomposition measure based on multi-layer sparsity for the multi-layer progressive regularization of tensor sparsity information. Meanwhile, in order to solve the shortcoming of Tucker decomposition, Bu et al. [57] have integrated the graph Laplacian regularizations imposed on factor matrices in the multilinear space and Tucker decomposition into a unified fusion framework.

Some other small target detection methods exist, but they all have some defects. The 3D matched filter [10], multiscan adaptive matched filter [13], max-mean/max-median filter [11], and improved 3D filter [12] are early detection methods for small targets. These methods require considerable prior knowledge, and their performance is poor for images with large clutter. These methods strongly rely on local prior assumptions between the background and the target. For example, the target can be detected by comparing only one pixel or area with its neighboring pixels, i.e., weighted local difference measure [14], local contrast method [1] and multiscale patch-based contrast measure [15]. However, if the image has strong edges or other interference components, these local difference-based methods may no longer be suitable. Therefore, some fuzzy measurement methods, such as multichannel kernel fuzzy correlogram [16] and the multiscale fuzzy metric [17], have been proposed, but these methods also need prior information about the size of the target and have high computational complexity.

To overcome the drawbacks of these methods, in this paper, we propose a generalized low-rank double-tensor nuclear norm completion framework to detect small targets in infrared images. We focus on target enhancement and background recovery from the perspective of low-rank matrix recovery and local differences. We conduct a number of experiments to verify the accuracy of this method. The contributions of this paper are the following:

1): We propose to use the ring top-hat regularization term to reduce noise and clutter. In addition, to fully and locally utilize the structure between the low-rank background area and the target area, in contrast to the traditional morphological structure, we design a weighted ring structural element to detect small infrared targets.

2): To avoid destruction of the tensor data structure and internal correlation by data vectorization that occurs in traditional regularization, we introduce the Grassmann manifold low-rank model based on the double nuclear norm into the tensor model. The integrity of the structural features of the low-rank tensor is preserved, and the computational complexity is reduced.

3): We use the alternating direction multiplier method (ADMM) to solve the proposed infrared small target detection tensor model. And the experiment proves that our proposed method is superior to the comparison methods.

The rest of this paper is organized as follows. We introduce some preliminaries for tensors and the definition of morphological regularization in Section 2. We present and analyze

our model in Section 3. Then, we introduce the concrete solution steps of our model in Section 4. Finally, we conduct many experiments from various aspects and prove the superior performance of our model in Section 5.

II. PRELIMINARIES

The pixels in infrared images are highly correlated, and the background is represented in a continuous manner. Compared with the low-rank surrounding background, the target is prominent and sparse, which destroys the local correlation of the infrared image. Therefore, we can separate the target from the surrounding background via matrix completion, and tensor information can be explored to further highlight the targets and the complex background as much as possible. Low-rank tensor recovery belongs to the spatial domain and is easy to realize.

A. Low-Rank-Based Small Target Detection

To characterize our model, we denote the original infrared image as G^D. Clearly, G^D consists of the target (G^T), background (G^B) and noise (G^N), so our infrared model is expressed as follows:

$$G^D = G^T + G^B + G^N \qquad (1)$$

From the inherent spatial correlation between the pixels in infrared images, it can be seen that the background (G^B is expressed in a continuous manner and has strong local correlation, but the characteristic target (G^T) is the object that breaks this correlation. To segment the target (G^T), background (G^B), and noise (G^N) from the input infrared image (G^D), we can apply low-rank matrix completion to the continuous background [34]. The completion is performed according to the low-rank correlation characteristics of the background and the sparsity of the target . Although the rank minimization problem is NP-hard, we can still easily find an alternative method for the rank function and the kernel norm, for example, sparse representation of the low-rank matrix.

B. Notation and Definition of Tensor Nuclear Norm

Before introduce low-rank tensor recovery in detail, we first define some mathematical notations in Table I.

In the frequency domain, $\hat{\mathcal{G}}$ can be represented by block-diagonal matrix form $\bar{\mathcal{G}}$, then:

$$\bar{\mathcal{G}} \triangleq blockdiag\left(\hat{\mathcal{G}}\right) \triangleq \begin{bmatrix} \hat{\mathcal{G}}^{(1)} & & & \\ & \hat{\mathcal{G}}^{(2)} & & \\ & & \ddots & \\ & & & \hat{\mathcal{G}}^{(n_3)} \end{bmatrix} \qquad (2)$$

where $\hat{\mathcal{G}} \in \mathbb{R}^{n_1 n_3 \times n_2 n_3}$, and $\hat{\mathcal{G}}^{(k)}$ is the k-th frontal slice of $\hat{\mathcal{G}}$.

Then we have the nature:

$$\mathcal{A} * \mathcal{B} = \mathcal{C} \Leftrightarrow \bar{\mathcal{A}} \cdot \bar{\mathcal{B}} = \bar{\mathcal{C}}$$

where $\cdot$ is the matrix product.

Now, we can introduce the tensor-nuclear-norm [38](TNN) $\|\cdot\|_{TNN}$

TABLE I
NOTATION AND DEFINITION

Notation	Definition
G	Matrix
$\mathcal{G} \in \mathbb{R}^{I_1 \times I_2 \times \ldots \times I_N}$	N-dimensional tensors with the size $I_1, I_2, , \ldots, I_N \in \mathbb{N}$ in each dimension
$g_{i_1 \times i_2 \times \ldots \times i_N}$	The $(i_1, i_2, \ldots, i_N)^{th}$ element of the tensor $\mathcal{G}$
$\langle \mathcal{G}^{\mathcal{D}} \cdot \mathcal{G}^{\mathcal{B}} \rangle = \sum_{i_1=1}^{I_1} \cdots \sum_{i_N=1}^{I_N} g_{d(i_1,\ldots,i_N)} g_{b(i_1,\ldots,i_N)}$	The inner product of tensors $\mathcal{G}^{\mathcal{D}}$ and $\mathcal{G}^{\mathcal{B}}$
$\|\mathcal{G}^{\mathcal{D}}\|_F = \sqrt{\langle \mathcal{G}^{\mathcal{D}} \cdot \mathcal{G}^{\mathcal{D}} \rangle}$	Frobenius norm of tensor $\mathcal{G}^{\mathcal{D}}$
$\mathcal{G}(1, \ldots, i, \ldots, I_n)$	The mode-n fibre of tensor $\mathcal{G}$, where $1 \leq i \leq I_n$
$G_{(n)}$	The mode-n unfolding matrix of tensor $\mathcal{G}$, where $1 \leq n \leq N$
$G_{(n)} = unfold_n(\mathcal{G}^n)$	The mode-n unfolding of tensor $\mathcal{G}$
$\mathcal{G} = fold_n(G_{(n)})$	The inverse operator of $unfold()$

$$\|\mathcal{G}\|_{TNN} \triangleq \|\bar{\mathcal{G}}\|_* = \sum_{i=1}^{n_3} \left\|\hat{\mathcal{G}}^{(i)}\right\|_* \qquad (3)$$

where $\|\cdot\|_*$ is matrix nuclear norm.

C. Definition of Morphological Regularization

At present, morphological detection is widely used in the detection of small targets in infrared images. In classic morphological theories, corrosion and expansion are the most basic operators. Structural elements are equivalent to those involved in filtering a template; that is, a matrix of a given pixel can be of any shape, generally square or circular. The design of the operators and structural elements is crucial in infrared small target detection based on morphology. Currently, the top-hat operator is popular for detecting small targets in infrared images.

We first introduce relevant knowledge about the two basic operations of expansion and corrosion, which use original images and structural elements. Let I represent a grayscale image and S represent a structural element. We define dilation as $I \oplus S$ and define erosion as $I \ominus S$ of $I(x, y)$ by $S(a, b)$:

$$(I \oplus S)(x, y) = \max_{a,b} (I(x - a, y - b) + S(a, b)) \qquad (4)$$

$$(I \ominus S)(x, y) = \min_{a,b} (I(x + a, y + b) - S(a, b)) \qquad (5)$$

where the domains of $I \oplus S$ and $I \ominus S$ are the dilation and erosion of the domain of I with the domain of S. The opening and closing operations represented by I and S can be expressed as:

$$(I \circ S)(x, y) = (I \ominus S) \oplus S \qquad (6)$$

$$(I \bullet S)(x, y) = (I \oplus S) \ominus S \qquad (7)$$

where the opening operation and the closing operation are represented by $(I \circ S)$ and $(I \bullet S)$, respectively; $(I \circ S)$ (or

$(I \bullet S)$) is often used to smooth images with noise. The classic top-hat transformations, namely, white top-hat transformation (WTHT) and black top-hat transformation (BTHT), are defined by Eq.8 and Eq.9.

$$WTHT(x,y) = I(x,y) - (I \circ S)(x,y) \qquad (8)$$

$$BTHT(x,y) = (I \bullet S)(x,y) - I(x,y) \qquad (9)$$

The structural element is an important concept in mathematical morphology, and it is a basic unit used to corrode and expand images. In an infrared image, the object to be detected usually differs substantially from the surrounding background area, and there are strong edge differences. Therefore, the different information provided by the small target and the background can be used to distinguish the background and the target. The basis of using the top-hat transform for small target detection is to use this different information to detect the target.

III. THE PROPOSED METHOD

To solve the problem of minimizing convex optimization for Gaussian noise, we propose a target detection task using morphological operators and the low-rank background as constraints, in which we superimpose continuous multiple frames of images as input images ($\mathcal{G}^D$) into the tensor. First, we introduce morphological operators with ring structure elements. Then, we introduce the entire method of object detection. In the next section, we discuss our optimization process and algorithm flow in detail.

A. The Ring Structural Element for Top-Hat Regularization Transformation

Two identical structural elements are typically used in classical morphological theories, which ignore the difference between the target and the surrounding background. Similarly to the transformation of the classic top-hat operator, it performs the opening operation or the closing operation using two identical structural elements. The existing difference information is not appropriately considered in the structural elements, which may reduce the efficiency and accuracy, while the classic top-hat transformation distinguishes the target and the background. In our model, the difference areas between the target and the surrounding background are considered; we build a ring structural element composed of two structural elements with the same shape but different sizes to highlight the small targets, which is shown in detail in Figure 1.

Corrosion and expansion are the two basic operations in mathematical morphology. They work with the original image and the structural element. Here, let r_{E_i} and r_{E_o} represent the sizes of structural elements E_i and E_o, respectively, where r_{E_i} is smaller than r_{E_o}. Then, we define the difference between the two structural elements as the ring structural element, named RE, and set $r_{RE} = r_{E_o} - r_{E_i}$. r_{RE} is the radial distance of ring structure element RE. Additionally, we define the E_m as the ring structural element, which is larger than r_{E_i} and smaller than r_{E_o}. Thus, we can define the ring opening operation as $I < S$ and the closing operation as $I > S$:

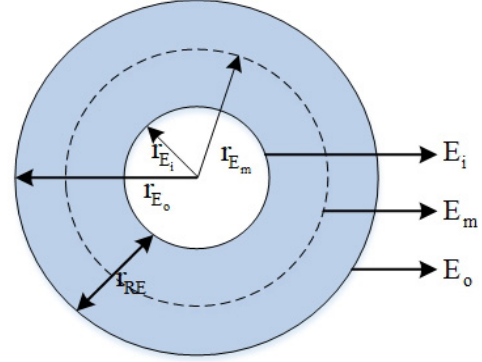$$(I < S)(x,y) = (I \oplus RE)\ominus E_m \qquad (10)$$

Fig. 1. Relationship of the structural elements

$$(I > S)(x,y) = (I\ominus RE) \oplus E_m \qquad (11)$$

Then, we define the top-hat regularization transformation as follows:

$$M(x,y) = I(x,y) - (I < E_{\text{guide}})(x,y) \qquad (12)$$

where E_{guide} is the structural elements. For the model of the tensor, we describe the top-hat regularization transformation as:

$$M(\mathcal{G}^{\mathcal{T}}) = \mathcal{G}^{\mathcal{T}}(x,y) - (\mathcal{G}^{\mathcal{T}} < E_{\text{guide}})(x,y) \qquad (13)$$

B. Infrared Small Target Detection Model Based on Low-Rank Double-Tensor Nuclear Norm

Due to the linearly correlation with each patches, we further exploit the low rank property of background. From the Fig. 2, we can explicitly find the truth that the singular value of corresponding background decrease rapidly to the zero. According to the related discussion, the background image ($\mathcal{G}^B$) can be considered a low-rank matrix, and we can assume the Eq.14.

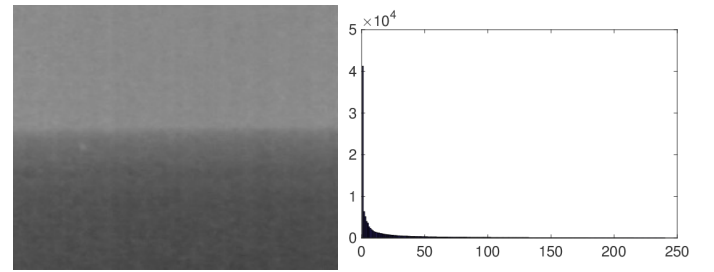$$\text{rank}(G^B) < k \qquad (14)$$

Fig. 2. The low rank illustration of background (left) can be explicit shown by the singular value in sub-figure (right).

Parameter k is determined by the sparsity of the input image. The more sparse the image is or the more uniform the image is, the smaller the value of k is. However, due to the existence of the target, the value of k is always larger than the value of the rank under a completely uniform background. Moreover, rank minimization is always an NP-hard problem, and low-rank tensors are more complicated.

The data to be processed here is a high-order sparse tensor. For the rank minimization problem, the single kernel norm is usually used to relax the rank function. Gao et al. constructed a local patch to transform the traditional infrared small target detection problem into a low-rank sparse matrix recovery problem [37]. Sun et al. proposed an infrared patch tensor model based on the weighted tensor kernel norm [38], which used the tensor kernel norm to restore the background to isolate the target. However, the low rank subproblem based on kernel norm will make the rank components over relax from the representation matrix, resulting in the suboptimal solution deviating from the original solution. Schatten-p norm is often used to deal with the rank minimization problem of high-order sparse tensors [58] [59]. Which is formally more flexible than the nuclear norm and can better deal with many low-rank problems. If $0 < p < 1$, schatten-p norm can weaken the proportion of larger singular values in the objective function compared with kernel norm, which makes schatten-p norm more suitable for describing the rank minimization problem. However, the calculation of schatten-p norm is complex and takes a long time. Piao et al. proposed a Grassmann manifold low-rank model based on the dual-core norm [43]. They decomposed the matrix into the product of two low-rank matrices, and used the decomposition matrix as a constraint. The kernel norm is used to approximate the minimized rank of the original matrix. Experiments show that the low-rank Grassmann manifold model based on the Double-Tensor Nuclear norm can make better use of the local geometric structure of the data space. Therefore, in order to seek the balance between efficiency and accuracy, we use the double nuclear norm, a kind of schatten-p-quasi-norm, to approximate rank minimization.

Based on the above analysis, we rewrite the objective function of Eq.14, then represent the double nuclear norm-based low-rank model as below:

$$\min_{X,A,B} \|A\|_* + \|B\|_* \\ s.t. \quad X = AB \tag{15}$$

where $\|A\|_* + \|B\|_*$ is the double nuclear norm of X and $A \in \mathbb{R}^{m \times r}$, $B \in \mathbb{R}^{r \times n}$. r is the expected rank of X, and $r < \min(m,n)$. Since it is difficult for a two-dimensional infrared image matrix to retain all the priors between the background and the target, to make full use of this prior, we use continuous frames of pictures as the input image tensor to preserve the structural features as much as possible, which can improve the accuracy of infrared small target detection. According to the definition of a tensor, a tensor composed of a plurality of continuous two-dimensional matrices can be represented by the unfolding matrix ($\mathcal{G}^{B(i)}$) of each mode. These mode-expanded matrices are considered low-rank matrices defined as:

$$\text{rank}(\mathcal{G}^{B(i)}) < k_{(i)} \tag{16}$$

where $\mathcal{G}^{B(i)}$ is the i-th mode expansion of tensor $\mathcal{G}^B$, $k_{(i)}$ are constants determined by the matrix, which represent the

unfolding of the tensor. Applying the double nuclear norm to the tensor model, Eq.15 can be written as:

$$\min_{\mathcal{G}^B, A, B} \sum_{i=1}^{3} (\|A_i\|_* + \|B_i\|_*) \\ s.t. \quad \mathcal{G}^{B(i)} = A_i B_i, \tag{17}$$

C. The Noise $\mathcal{G}^N$

In our model, we assume that the noise is random, and $\|G^N\|_F \le \delta$, $\delta > 0$. Thus, we can obtain:

$$\|G^D - G^T - G^B\|_F \le \delta \tag{18}$$

where $\|\mathbf{g}\|_F$ is the Frobenius norm and $\|G^N\|_F = \sqrt{\sum_{ij} (G^N)_{ij}^2}$. In this tensor model, we can write the noise estimate as:

$$\|\mathcal{G}^D - \mathcal{G}^T - \mathcal{G}^B\|_F \le \delta \tag{19}$$

The process of our model is shown in Fig. 3. First, we construct a tensor based on the original input infrared images. Second, to restore the target image, we enforce the top-hat regularization on the input images. Third, to restore the background image, we apply a double nuclear norm to the low-rank matrix model. Our model can be efficiently solved by ADMM. We present the details of our algorithm in Algorithm 1.

IV. THE ALGORITHM FOR SMALL TARGET DETECTION

A. Model Formulation

In this part, we introduce our infrared small target detection model. We assume that the noise in the images is random. Therefore, the model can be written as:

$$\min_{\mathcal{G}^B, \mathcal{G}^T} \alpha \sum_{i=1}^{3} u_i (\|A_i\|_* + \|B_i\|_*) + \beta M(\mathcal{G}^T) \\ s.t. \quad \mathcal{G}^{B(i)} = A_i B_i, \|\mathcal{G}^D - \mathcal{G}^T - \mathcal{G}^B\|_F \le \varepsilon \tag{20}$$

where $\mathcal{G}^D$, $\mathcal{G}^N$, $\mathcal{G}^B$, and $\mathcal{G}^T$ are the original infrared image, the noise image, the background image, and the target image, u_i is the weight of i-th dimension in the tensor, α, β and ε are constants, and A_i and B_i represent the expected rank of the background image. $M(\mathcal{G}^T)$ is the morphological regularization term.

Model (20) can be transformed into:

$$\min_{\mathcal{G}^N, \mathcal{G}^B, \mathcal{G}^T} \frac{1}{2} \|\mathcal{G}^N\|_F^2 + \alpha \sum_{i=1}^{3} u_i (\|A_i\|_* + \|B_i\|_*) + \beta M(\mathcal{G}^T) \\ s.t. \quad \mathcal{G}^T + \mathcal{G}^B + \mathcal{G}^N = \mathcal{G}^D, \mathcal{G}^B = \mathcal{Y}_i, \mathcal{Y}_{i(i)} = A_i B_i \tag{21}$$
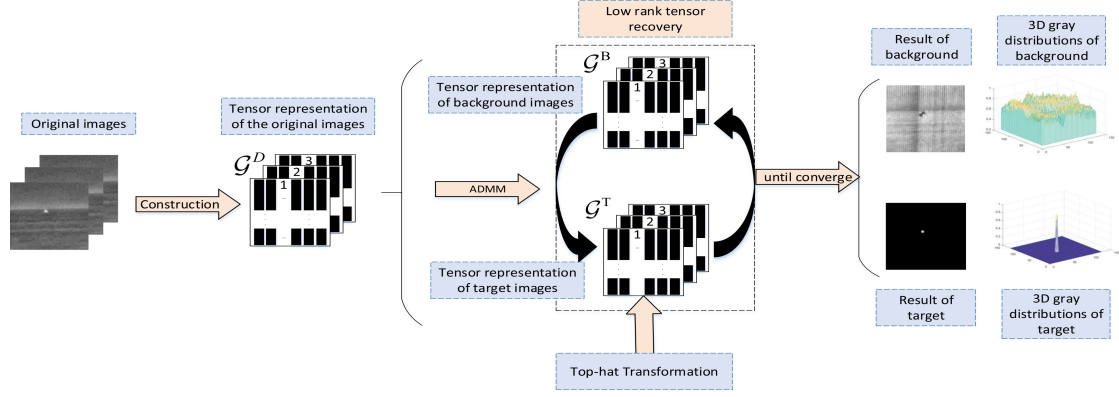
Fig. 3. The algorithm of our proposed model

We solve the eq.21 by the alternating direction multiplier method (ADMM); the model can be written as:

$$L\left(\mathcal{G}^N, \mathcal{G}^B, \mathcal{G}^T, A_i, B_i\right)$$

$$=\frac{1}{2}\left\|\mathcal{G}^N\right\|_F^2 + \alpha \sum_{i=1}^3 u_i\left(\|A\|_* + \|B\|_*\right) + \beta M\left(\mathcal{G}^T\right)$$

$$- \left\langle \mathcal{G}^Z, \mathcal{G}^T + \mathcal{G}^B + \mathcal{G}^N - \mathcal{G}^D\right\rangle - \sum_{i=1}^3\left\langle \mathcal{S}_i, \mathcal{G}^B - \mathcal{Y}_i\right\rangle$$

$$- \sum_{i=1}^3\left\langle L_i, A_i B_i - \mathcal{Y}_{i(i)}\right\rangle + \sum_{i=1}^3\frac{\rho_i}{2}\left\|\mathcal{G}^B - \mathcal{Y}_i\right\|_F^2 \qquad (22)$$

$$+ \frac{a}{2}\left\|\mathcal{G}^T + \mathcal{G}^B + \mathcal{G}^N - \mathcal{G}^D\right\|_F^2$$

$$+ \sum_{i=1}^3\frac{\sigma_i}{2}\left\|A_i B_i - \mathcal{Y}_{i(i)}\right\|_F^2$$

where L_i and $\mathcal{S}_i$ are Laplace factors and ρ_i and σ_i are penalty factors.

B. Optimization

In this section, we adopt ADMM to solve the problem in detail.

1) Update noise

We assume that other variables are fixed, and the noise solution is described below:

$$\min_{\mathcal{G}^N}\frac{1}{2}\left\|\mathcal{G}^N\right\|_F^2 - \left\langle \mathcal{G}^Z, \mathcal{G}^T + \mathcal{G}^B + \mathcal{G}^N - \mathcal{G}^D\right\rangle$$
$$+ \frac{a}{2}\left\|\mathcal{G}^T + \mathcal{G}^B + \mathcal{G}^N - \mathcal{G}^D\right\|_F^2 \qquad (23)$$

(23) can be rewritten as:

$$\min_{\mathcal{G}^N}\frac{1}{2}\left\|\mathcal{G}^N\right\|_F^2 + \frac{a}{2}\left\|\mathcal{G}^T + \mathcal{G}^B + \mathcal{G}^N - \mathcal{G}^D - \frac{\mathcal{G}^Z}{a}\right\|_F^2 \qquad (24)$$

We update the noise by:

$$\mathcal{G}^N = \frac{1}{a+1}\left(\mathcal{G}^Z - a\left(\mathcal{G}^T + \mathcal{G}^B - \mathcal{G}^D\right)\right) \qquad (25)$$

2) Update Target

We assume that other variables are fixed, and the solution of the target can be described below:

$$\min_{\mathcal{G}^T}\beta M\left(\mathcal{G}^T\right) + \frac{a}{2}\left\|\mathcal{G}^T + \mathcal{G}^B + \mathcal{G}^N - \mathcal{G}^D - \frac{\mathcal{G}^Z}{a}\right\|_F^2 \qquad (26)$$

Here, we write the corresponding iteration as:

$$\mathcal{G}^{T(n+1)} = \mathcal{G}^{D(n+1)} + \frac{\mathcal{G}^Z}{a} - \mathcal{G}^{N(n+1)} - \mathcal{G}^{B(n+1)}$$
$$- \frac{\beta}{a}\left(\frac{\delta}{\delta\left(\mathcal{G}^T\right)}M\left(\mathcal{G}^T\right)\right)_{\mathcal{G}^{T(n)}} \qquad (27)$$

where $\left(\frac{\delta}{\delta\left(\mathcal{G}^T\right)}M\left(\mathcal{G}^T\right)\right)$ is the subgradient of the structural element operator. We use the ring top-hat operator, so this subgradient can be written as follows:

$$\frac{\delta}{\delta\left(\mathcal{G}^T\right)}M\left(\mathcal{G}^T\right)$$

$$= \mathcal{G} - \frac{\delta}{\delta\left(\mathcal{G}^T\right)}E_{E_m}\left(D_{RE}\left(\mathcal{G}^T\right)\right) \qquad (28)$$

$$= \mathcal{G} - \frac{\delta D_{RE}\left(\mathcal{G}^T\right)}{\delta\left(\mathcal{G}^T\right)}\frac{\delta E_{E_m}\left(D_{RE}\left(\mathcal{G}^T\right)\right)}{\delta D_{RE}\left(\mathcal{G}^T\right)}$$

We define the subgradient of the dilated and eroded operations as $\delta D_{RE,j}/\delta t_i$ and $\delta E_{E_m,j}/\delta t_i$, respectively, and the subgradient of the j-th element of the i-th column can be calculated as:

$$\frac{\delta D_{RE,j}}{\delta p_i} = \begin{cases} 1, & \text{if } p_i = \max_{g\in(RE_{\text{guide}})(j)}\{p_g\} \\ 0, & \text{if } p_i < \max_{g\in(RE_{\text{guide}})(j)}\{p_g\} \end{cases} \qquad (29)$$

$$\frac{\delta E_{E_m,j}}{\delta p_i} = \begin{cases} 1, & \text{if } p_i = \min_{g\in(E_m\text{guide})(j)}\{p_g\} \\ 0, & \text{if } p_i > \min_{g\in(E_m\text{guide})(j)}\{p_g\} \end{cases} \qquad (30)$$

where RE and E_m store the pixel values of the coverage area in $RE_{\text{guide}}(j)$ and $E_{m\text{guide}}(j)$, respectively.

We first dilate the image and then erode the dilated image. We define the dilated image as $D_{S_1}(X) = [d_{s1,1}, d_{s1,2}, L, d_{s1,mn}]$. Additionally,

$(\delta E_{E_m}(D_{RE}(\mathcal{G}^T)))/(\delta D_{RE}(\mathcal{G}^T))$ can be defined as follows:

$$\frac{\delta E_{E_m}(D_{RE}(\mathcal{G}^T))}{\delta D_{RE}(\mathcal{G}^T)} = \frac{\delta E_{E_m,j}}{\delta d_{RE,i}}$$
$$= \begin{cases} 1, & \text{if } d_{RE,i} = \min \mathrm{r} \in (E_{m\text{guide}})(j)\{d_{s1,r}\} \\ 0, & \text{if } d_{RE,i} > \min \mathrm{r} \in (E_{m\text{guide}})(j)\{d_{s1,r}\} \end{cases} \quad (31)$$

With (28), (29), (30) and (31), we can calculate $\mathcal{G}^{T(n+1)}$.

3) Update Background

If the other variables are fixed, the solution of the background can be written as follows:

$$\min_{\mathcal{G}^B} \quad \frac{a}{2}\left\|\mathcal{G}^T + \mathcal{G}^B + \mathcal{G}^N - \mathcal{G}^D - \frac{\mathcal{G}^Z}{a}\right\|_F^2$$
$$+ \sum_{i=1}^{3}\frac{\rho_i}{2}\left\|\mathcal{G}^B - \mathcal{Y}_i - \frac{\mathcal{S}_i}{\rho_i}\right\|_F^2 \quad (32)$$

We update the background by:

$$\mathcal{G}^B = \frac{a(\mathcal{G}^D - \mathcal{G}^T - \mathcal{G}^N) + \mathcal{G}^Z + \sum_{i=1}^{3}(\rho_i\mathcal{Y}_i + \mathcal{S}_i)}{a + \rho_1 + \rho_2 + \rho_3} \quad (33)$$
$$i = 1, 2, 3$$

4) Update others

If $\mathcal{G}^D$, $\mathcal{G}^T$, $\mathcal{G}^B$, $\mathcal{G}^N$ are fixed, the solution of the double nuclear norm in eq.(22) can be described below:

$$\min_{A_i, B_i, \mathcal{Y}_i} \alpha u_i(\|A_i\|_* + \|B_i\|_*) - \langle \mathcal{S}^i, \mathcal{G}^B - \mathcal{Y}_i \rangle$$
$$+ \frac{\rho_i}{2}\|\mathcal{G}^B - \mathcal{Y}_i\|_F^2 - \langle L_i, A_iB_i - \mathcal{Y}_{i(i)} \rangle \quad (34)$$
$$+ \frac{\sigma_i}{2}\|A_iB_i - \mathcal{Y}_{i(i)}\|_F^2$$

We can solve (34) by ADMM. First, we introduce two auxiliary variables $A_i = \hat{A}_i$ and $B_i = \hat{B}_i$; then, (34) can be rewritten as:

$$\min_{A_i, B_i, \mathcal{Y}_i} \alpha u_i(\|A_i\|_* + \|B_i\|_*) - \langle \mathcal{S}^i, \mathcal{G}^B - \mathcal{Y}_i \rangle$$
$$+ \frac{\rho_i}{2}\|\mathcal{G}^B - \mathcal{Y}_i\|_F^2 - \langle L_i, A_iB_i - \mathcal{Y}_{i(i)} \rangle \quad (35)$$
$$+ \frac{\sigma_i}{2}\|A_iB_i - \mathcal{Y}_{i(i)}\|_F^2$$
$$s.t. \quad A_i = \hat{A}_i, B_i = \hat{B}_i, i = 1, 2, 3$$

We use the augmented Lagrangian method as follows:

$$La\left(A_i, B_i, \hat{A}_i, \hat{B}_i, \mathcal{Y}_i\right)$$
$$= \alpha u_i\left(\|\hat{A}_i\|_* + \|\hat{B}_i\|_*\right) - \langle \mathcal{S}_i, \mathcal{G}^B - \mathcal{Y}_i \rangle + \frac{\rho_i}{2}\|\mathcal{G}^B - \mathcal{Y}_i\|_F^2$$
$$- \langle L_i, A_iB_i - \mathcal{Y}_{i(i)} \rangle - \langle \lambda_i, \hat{A}_i - A_i \rangle - \langle \beta_i, \hat{B}_i - B_i \rangle$$
$$+ \frac{\sigma_i}{2}\|A_iB_i - \mathcal{Y}_{i(i)}\|_F^2 + \frac{\omega_i}{2}\|\hat{A}_i - A_i\|_F^2 + \frac{\eta_i}{2}\|\hat{B}_i - B_i\|_F^2 \quad (36)$$

where $i = 1, 2, 3$, λ and β are Lagrangian multipliers, and ω and η are penalty parameters. In this section, $\mathcal{Y}_i$, A_i, $\hat{A}_i$, B_i, $\hat{B}_i$ can be solved by the following alternating iterations, and n denotes the current iteration step.

4.1) Update $\hat{A}_i$:

$$\min_{\hat{A}_i} \alpha u_i\left\|\hat{A}_i\right\|_* + \frac{\omega_i}{2}\left\|\hat{A}_i - \left(A_i + \frac{\lambda_i}{\omega_i}\right)\right\|_F^2 \quad (37)$$
$$i = 1, 2, 3$$

$$\hat{A}_i^{n+1} = U_1^{(n)}\max\left\{\Sigma_1^{(n)} - \frac{\alpha u_i^{(n)}}{\omega_i^{(n)}}, 0\right\}V_1^{(n)T} \quad (38)$$

The parameters $U_1^{(n)}$, $\sum_1^{(n)}$, and $V_1^{(n)}$ are generated from the singular value decomposition (SVD) of $A_i + \frac{\lambda_i}{\omega_i}$.

4.2) Update $\hat{B}i$:

$$\min_{\hat{B}_i} \alpha u_i\left\|\hat{B}_i\right\|_* + \frac{\eta_i}{2}\left\|\hat{B}_i - \left(B_i + \frac{\beta_i}{\eta_i}\right)\right\|_F^2 \quad (39)$$
$$i = 1, 2, 3$$

The minimizer:

$$\hat{B}_i^{n+1} = U_2^{(n)}\max\left\{\Sigma_2^{(n)} - \frac{\alpha u_i^{(n)}}{\eta_i^{(n)}}, 0\right\}V_2^{(n)T} \quad (40)$$

where $U_2^{(n)}$, $\sum_2^{(n)}$ and $V_2^{(n)}$ are obtained via the SVD of $B_i + \frac{\beta_i}{\eta_i}$.

4.3) Update A_i:

$$\frac{\omega_i}{2}\left\|A_i - \hat{A}_i + \frac{\lambda_i}{\omega_i}\right\|_F^2 + \frac{\sigma_i}{2}\left\|A_iB_i - \mathcal{Y}_{i(i)} + \frac{1}{\sigma_i}L_i\right\|_F^2 \quad (41)$$
$$i = 1, 2, 3$$

The minimizer:

$$A_i^{(n+1)} = \frac{1}{\sigma_i\omega_i}\left(P_1^{(n)} + P_2^{(n)}B_i^{(n)T}\right)\left(I_1 + B_i^{(n)}B_i^{(n)T}\right)^{-1} \quad (42)$$

Here, $P_1^{(n)} = \hat{A}_i^{(n)} - \lambda_i^{(n)}\omega_i^{(n)}$, $P_2^{(n)} = \mathcal{Y}_{i(i)}^{(n)} + \frac{1}{\sigma_i}L_i^{(n)}$, and $I_1 \in R^{r \times r}$ is the identity matrix.

4.4) Update B_i:

$$\min_{B_i} \frac{\eta_i}{2}\left\|B_i - \hat{B}_i + \frac{\beta_i}{\eta_i}\right\|_F^2 + \frac{\sigma_i}{2}\left\|A_iB_i - \mathcal{Y}_{i(i)} + L_i\right\|_F^2 \quad (43)$$
$$i = 1, 2, 3$$

The minimizer:

$$B_i^{(n+1)} = \frac{1}{\sigma_i\eta_i}\left(A_i^{(n)T}A_i^{(n)} + I_1\right)^{-1}\left(A_i^{(n)T}P_2^{(n)} + P_3^{(n)}\right) \quad (44)$$

Similarly, $P_3^{(n)} = \hat{B}_i^{(n)} - \frac{\beta_i^{(n)}}{\eta_i^{(n)}}$

4.5) Update $\mathcal{Y}_i$:

$$\min_{\mathcal{Y}_i} \frac{\rho_i}{2}\left\|\mathcal{Y}_i - \left(\mathcal{G}^B - \frac{\mathcal{S}_i}{\rho_i}\right)\right\|_F^2 + \frac{\sigma_i}{2}\left\|\mathcal{Y}_{i(i)} - \left(A_iB_i - \frac{L_i}{\sigma_i}\right)\right\|_F^2 \quad (45)$$
$$i = 1, 2, 3$$

The minimizer:

$$\mathcal{Y}_i = \frac{\sigma_i\left(\mathcal{G}^B - \frac{\mathcal{S}_i}{\rho_i}\right) + \rho_i fold_i\left(A_iB_i - \frac{L_i}{\sigma_i}\right)}{\rho_i + \sigma_i} \quad (46)$$

The mode-i unfolding matrix $T_{D(i)}$ of tensor $\mathcal{T}_D$ can be transformed back to the tensor by $\mathcal{T}_D = fold_i(T_{D(i)})$, here $i = 1, 2, 3$.

Algorithm 1   solution for proposed model

1: Step 1: **Input:** $\mathcal{G}^{\mathcal{D}}$

2: Step 2: **Initialize:** $\mathcal{G}^B = \mathcal{G}^D, \mathcal{Y}_i = \mathcal{G}^B, \mathcal{G}^N = 0, \mathcal{G}^T = 0, \mathcal{G}^{\mathcal{Z}} = 1$

3: Step 3: Do ring top-hat transformation on $\mathcal{G}^{\mathcal{D}}$ to achieve the $\frac{\delta D_{RE,j}}{\delta p_i}$ and $\frac{\delta E_{E_m,j}}{\delta d_{RE,i}}$

4: Step 4: **While** $\dfrac{\left\|\mathcal{G}^{T(n)}\right\|_F}{\left\|\mathcal{G}^{T(n+1)}\right\|_F} < 1$ (**not converge**) **or iter** < **maxiter do**

    Step 4.1: $\mathcal{G}^{N(n+1)} = \dfrac{1}{a+1}\left(\mathcal{G}^Z - a\left(\mathcal{G}^T + \mathcal{G}^B - \mathcal{G}^D\right)\right)$

    Step 4.2: $\mathcal{G}^{T(n+1)} = \mathcal{G}^{D(n+1)} + \dfrac{\mathcal{G}^Z}{a} - \mathcal{G}^{N(n+1)} - \mathcal{G}^{B(n+1)} - \dfrac{\beta}{a}\left(\dfrac{\delta}{\delta\left(\mathcal{G}^T\right)}M\left(\mathcal{G}^T\right)\right)_{\mathcal{G}^{T(n)}}$

    Step 4.3: $\mathcal{G}^{B(n+1)} = \dfrac{a\left(\mathcal{G}^D - \mathcal{G}^T - \mathcal{G}^N\right) + \mathcal{G}^Z + \sum_{i=1}^{3}\left(\rho_i \mathcal{Y}_i + \mathcal{S}_i\right)}{a + \rho_1 + \rho_2 + \rho_3}$

    for i = 1 to 3 do

    Step 4.4: $\hat{A}_i^{(n+1)} = U_1^{(n)}\max\left\{\Sigma_1^{(n)} - \dfrac{\alpha u_i^{(n)}}{\omega_i^{(n)}}, 0\right\}V_1^{(n)T}$

    Step 4.5: $\hat{B}_i^{(n+1)} = U_2^{(n)}\max\left\{\Sigma_2^{(n)} - \dfrac{\alpha u_i^{(n)}}{\eta_i^{(n)}}, 0\right\}V_2^{(n)T}$

    Step 4.6: $A_i^{(n+1)} = \dfrac{1}{\sigma_i \omega_i}\left(P_1^{(n)} + P_2^{(n)}B_i^{(n)T}\right)\left(I_1 + B_i^{(n)}B_i^{(n)T}\right)^{-1}$

    Step 4.7: $B_i^{(n+1)} = \dfrac{1}{\sigma_i \eta_i}\left(A_i^{(n)T}A_i^{(n)} + I_1\right)^{-1}\left(A_i^{(n)T}P_2^{(n)} + P_3^{(n)}\right)$

    Step 4.8: $\mathcal{Y}_i^{(n+1)} = \dfrac{\sigma_i\left(\mathcal{G}^B - \dfrac{\mathcal{S}_i}{\rho_i}\right) + \rho_i fold_i\left(A_i B_i - \dfrac{L_i}{\sigma_i}\right)}{\rho_i + \sigma_i}$

    end for

    Step 4.9: $\mathcal{G}^{Z(n+1)} = \mathcal{G}^{Z(n)} - a\left(\mathcal{G}^{N(n+1)} + \mathcal{G}^{B(n+1)} + \mathcal{G}^{T(n+1)} - \mathcal{G}^{D(n+1)}\right)$

5: Step 5: **Output:** $\mathcal{G}^B$, $\mathcal{G}^T$

V. Experimental results and discussion

In this section, we compare the performance of our method with that of other baseline methods. First, we introduce the datasets and weighted structural element we used. Then, we discuss the baseline methods and the evaluation metrics used for comparison in this paper. Finally, we demonstrate the performance on real image sequences.

A. Datasets and Parameters

In this section, we analyse the characteristics of six real image sequences and discuss the sharpness of the selected structural elements. Then, we compare the detection performance of the traditional structural elements and our structural elements in these six image sequences.

Datasets: Considering the diversity of targets and the complexity of the background in practical applications, we select six groups of sequences for the experiment, each of which is composed of multiple images. In sequence 1, the target to be detected is a regular-shaped ship travelling far away under a blurred sea-sky background. In sequence 2, the target is a helicopter with a regular shape flying in a complex sky. In sequence 3, the detected target is a stationary aircraft with a constantly changing shape surrounded by clouds. In sequence 4, the target to be detected is a ship with a regular shape at close range, sailing in a fuzzy sea and sky background. In sequence 5, the target is a regular-shaped truck, driving on a long bridge, and the edges of the body are almost blurred. In Sequence 6, the target is a ship moving rapidly against a background of mixed sea and sky, with its shape constantly changing. More information about each sequence is presented in Table II.

To observe the real image sequence intuitively, we select a frame from each sequence and display it, its 3D map and the detection results for six original images obtained by our method in Fig.4.

TABLE II
THE INFORMATION OF REAL IMAGE SEQUENCES

	Frames	Image size	Target size
seq1	997	320×196	$4 \times 4 \sim 5 \times 5$
seq2	598	320×196	$4 \times 6 \sim 5 \times 6$
seq3	372	128×128	$5 \times 6 \sim 5 \times 8$
seq4	998	128×128	$4 \times 4 \sim 5 \times 5$
seq5	69	320×240	$3 \times 4 \sim 4 \times 5$
seq6	787	128×128	$6 \times 10 \sim 17 \times 43$

Parameter Settings: In this paper, RE is the ring structural element, which is determined by E_O and E_i. To balance the goal and the background, E_O is one or two pixels larger than the target, and E_i is one or two pixels smaller than the target. For sequences with targets that change in size, we select the structural element based on the smallest target.

To facilitate the construction of structural elements, we select rectangular rather than circular structural elements, as shown in Fig.5. The value of the structural element is defined as:

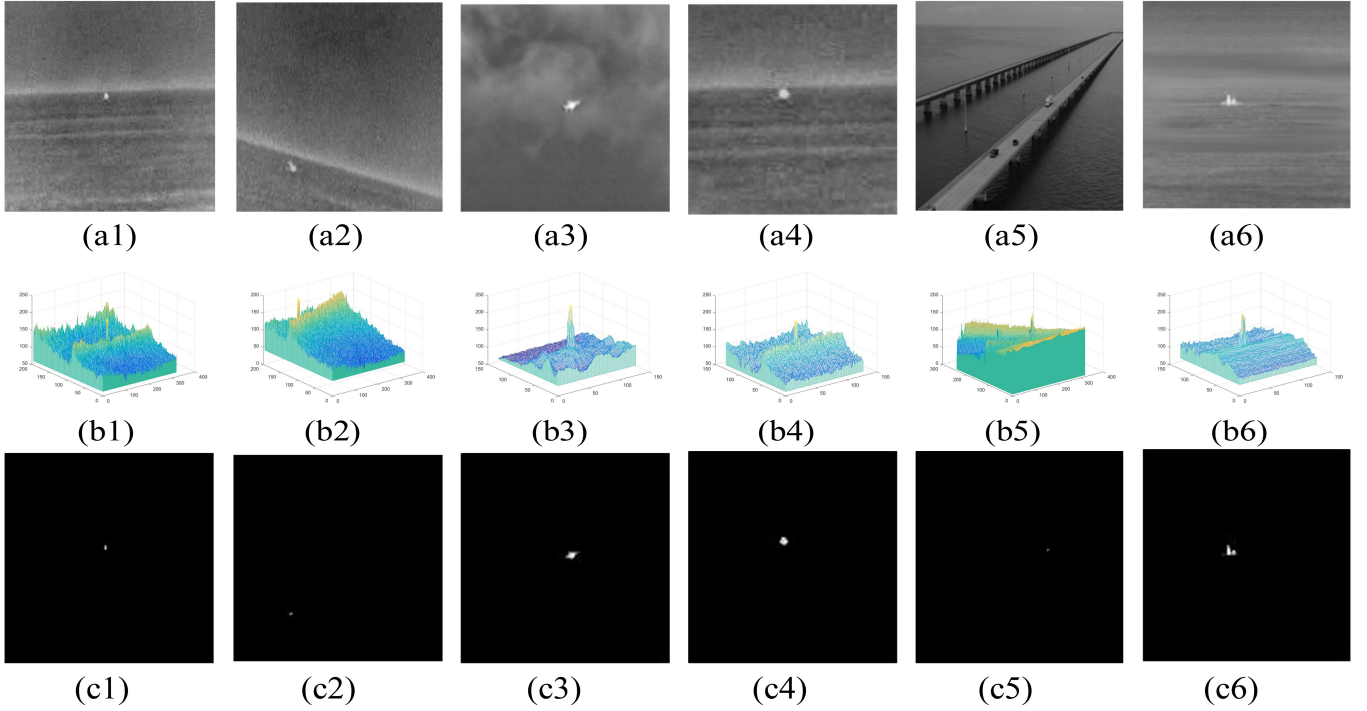$$v_{ij} = \frac{(p_{ij} - E)(C - E)}{D + eps} + 1 \tag{47}$$

Fig. 4. Real images and detected results. (a1)-(a6) are the infrared images of each sequence, (b1)-(b6) are the corresponding three-dimensional gray distributions, and (c1)-(c6) are the corresponding detection results of our method.
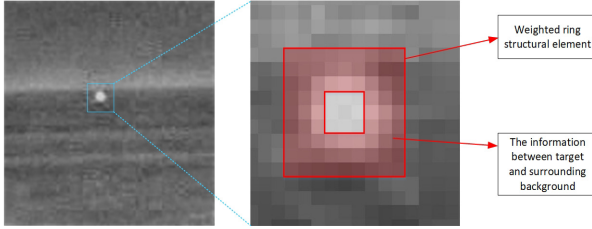

Fig. 5. Our proposed structural elements.

where v_{ij} is the value of each pixel in the structural element. We define y as a small image that belongs to $\mathcal{G}^D$ to be processed by the current structural element. p_{ij} is the value of each pixel in y, E is the mathematical expectation of y, C is the value of the centre pixel in y, and D is the variance of y. We define the size of the structural elements as $m \times n$, so $1 \le i \le m$, and $1 \le j \le n$.

B. Evaluation Metrics and Baseline Methods

Evaluation Metrics. To illustrate the superiority of our method, we choose five metrics: background suppression factor (BSF), signal-to-clutter ratio gain (SCRG), probability of detection (Pd), false alarm rate (Fa) and area under the curve (AUC).

$$BSF = \frac{\text{standard deviation of input image}}{\text{standard deviation of output image}} \quad (48)$$

$$SCRG = \frac{\frac{\text{average value of the pixels in input image}}{\text{standard deviation of input image}}}{\frac{\text{average value of the pixels in output image}}{\text{standard deviation of output image}}} \quad (49)$$

In small target detection performance evaluation, BSF and SCRG are often used to evaluate the performance of suppression of the background and the enhancement effect on small targets, respectively. A larger BSF indicates better suppression of the background, and a larger SCRG indicates better enhancement of small targets.

$$Pd = \frac{\text{number of correctly detected targets}}{\text{number of actual targets to be detected}} \quad (50)$$

$$Fa = \frac{\text{number of falsely detected targets}}{\text{number of images to be detected}} \quad (51)$$

The key metrics used to evaluate the performance of small target detection methods are Pd and Fa. A larger Pd and smaller Fa indicate that the method can detect small targets more accurately. In this paper, we compare the position of the brightest pixel in the real target and the detected target. If the distance does not exceed 5 pixels, we consider the target to be detected.
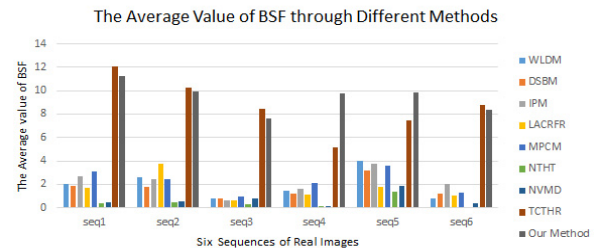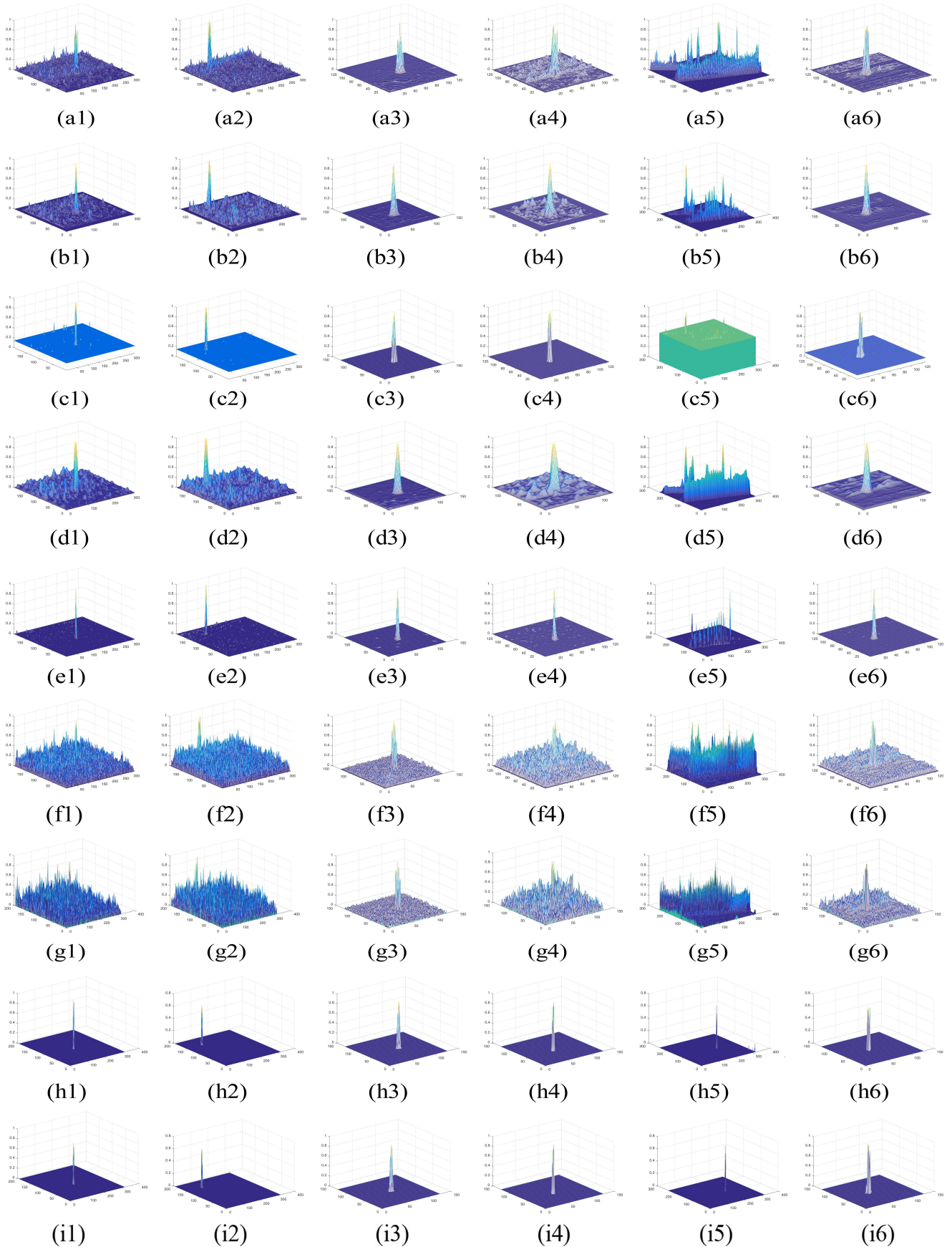

Fig. 7. The BSF of different methods.

Fig. 6. 3D gray distribution of detection results from different baseline methods. (a1)-(a6) WLDM, (b1)-(b6) DSBM, (c1)-(c6) IPM, (d1)-(d6) STSA, (e1)-(e6) MPCM, (f1)-(f6) NTHT, (g1)-(g6) NVMD, (h1)-(h6) TCTHR and (i1)-(i6) our method.
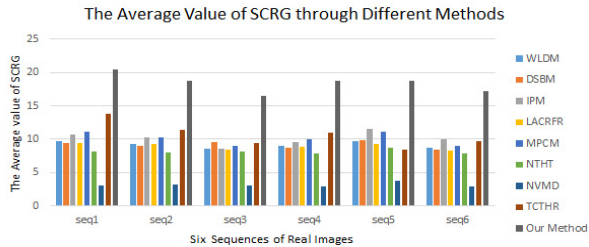
Fig. 8. The SCRG of different methods.

AUC, the area under the receiver operating characteristic (ROC) curve, is used to compare different classification models. Its value is between 0-1. A larger AUC means the method has better performance. The abscissa of the ROC curve is Fa, and vertical coordinate is Pd.

Baseline Methods. Next, we introduce several baseline methods that we use for comparison.

- **Weighted local difference measure (WLDM) [14]:** WLDM detects small targets with a weighted local difference measure map.
- **Directional saliency-based method (DSBM) [45]:** DSBM uses an SODD filter to decompose the original image into two orthogonal direction groups. It uses PFT to compute the directional saliency maps and obtains the target-saliency map by saliency fusion.
- **Infrared patch image model (IPM) [37]:** IPM transforms the input image into an infrared patch image model, and realizes small target detection by solving the problem of low-rank and sparse tensor recovery.
- **Spatio-temporal saliency approach (STSA) [44]:** STSA obtains the saliency map in time and space by means of a local adaptive contrast operation and combines the motion consistency characteristic of the moving target to realize small target detection.
- **Multiscale patch-based contrast measure (MPCM) [8]:** MPCM divides the image into multiscale images, and forms the final contrast image according to the maximum value of the local contrast pixels between different scales to enhance the contrast between the target and background.
- **New top-hat transform (NTHT) [36]:** NTHT changes the classic structural elements into two different but related structural elements to compare the differences between the surrounding area and the target.
- **Non-negativity-constrained variational mode decomposition (NVMD) [46]:** TCTHR uses the idea of tensor completion, adds morphological regularization constraints to the objective function, and uses schatten-p norm approximate rank minimization to achieve small target detection.
- **Tensor Completion With Top-Hat Regularization (TC-THR) [47]:** TCTHR decomposes the input image into several separate band-limited signals and uses the non-negative constraint. The infrared target is extracted from the corresponding target sub-region.

C. Detection Results

In this section, we present the 3D gray distribution of detection results obtained through different methods to illustrate the superior performance of our method.

We compare WLDB [14], DSBM [45], IPM [37], STSA [44], MPCM [8], NTHT [36], NVMD [46], TCTHR [47] and our method on six sequences of real images. To show the experimental results of different methods intuitively, we display these results in Fig.6, corresponding to the pictures in Fig.4, in the form of 3D distributions. Our method has the least clutter for all six real image sequences, especially for seq5, which indicates that our method has a stronger suppression effect on the background. Compared with NVMD, which uses the top-hat transformation, our method greatly enhances the background suppression effect, which indicates that the recovery part of the low-rank tensor plays an important role. Compared with IPM, which just uses low-rank matrix recovery, our method is more effective on background suppression, which indicates that the morphological regularization and double nuclear norm also enhance the detection performance.

D. Performance Analysis

In this section, we use several metrics, including SCRG, BSF, Pd, Fa, ROC plot and AUC values, to compare the performance of our method with that of other methods.

First, we compare the BSF and SCRG of different methods as column charts in Fig.7 and Fig.8. The SCRG of our method are the largest for all six sequences, and the BSF of our method are not always the largest, but it is not much different from the largest, which indicates that our method has a better enhancement effect on the target and a stronger suppression effect on the background. Therefore, from the perspective of SCRG and BSF, our method performs the best on these six real image sequences.

We also calculate the corresponding Pd and Fa in Table III, and plot the ROC in Fig. 9. The corresponding AUC of each method is recorded in Table IV. Our proposed method always has the highest Pd and lowest Fa, except on seq4 and seq6, and the AUC value of our method is always the largest, which indicates that our method can detect the whole target better. By using the weighted ring top-hat structural element regulization and double nuclear norm, we take full advantage of the differences between the target and surrounding background and improve the rank minimization, so we achieve the maximum Pd and AUC and the smallest Fa. In addition, other methods cannot maintain a satisfactory detection rate and false alarm rate for different sequences. Therefore, our method detects the target most accurately and completely in these six sequences.

Finally, we compare the performance of traditional structural elements and weighted ring structural elements on six sequences of real images and calculate the Pd and Fa values, which are recorded in Table VI. Weighted ring structural elements yield better detection performance, which proves that weighted ring structural elements use the difference information between the target and its surrounding background more effectively.

12

TABLE III
Pd AND Fa OF DIFFERENT METHODS

	WLDM		IPM		DSBM		STSA		MPCM		NTHT		NVMD		TCTHR		Our Method	
	Pd	Fa	Pd	Fa	Pd	Fa	Pd	Fa	Pd	Fa	Pd	Fa	Pd	Fa	Pd	Fa	Pd	Fa
seq1	0.831	0.170	0.851	0.149	0.864	0.179	0.857	0.143	0.858	0.142	0.845	0.245	0.757	0.243	0.859	0.141	**0.877**	**0.123**
seq2	0.445	0.555	**0.334**	0.666	0.729	0.339	0.363	0.637	0.726	0.274	0.507	0.684	0.393	0.607	0.799	0.201	**0.808**	**0.192**
seq3	0.884	0.116	0.704	0.296	0.978	0.102	0.973	0.027	0.941	0.059	0.938	0.159	0.847	0.153	0.949	0.051	**0.981**	**0.019**
seq4	0.846	0.154	0.957	0.043	0.977	0.056	**0.990**	**0.010**	0.974	0.026	0.966	0.123	0.966	0.034	0.962	0.038	0.980	0.019
seq5	0.174	0.826	0.783	0.217	0.754	0.261	0.130	0.870	0.826	0.174	0.159	0.855	0.290	0.710	0.812	0.188	**0.913**	**0.087**
seq6	0.431	0.569	0.390	0.610	0.726	0.296	0.665	0.335	0.705	0.295	0.563	0.518	0.386	0.614	**0.813**	**0.186**	0.762	0.238

TABLE IV
THE VALUES OF AUC OBTAINED BY DIFFERENT METHODS

	WLDM	IPM	DSBM	STSA	MPCM	NTHT	NVMD	TCTHR	Our Method
seq1	0.9799	0.9775	0.9662	0.9778	0.9487	0.9818	0.9511	0.9687	**0.9949**
seq2	0.9752	0.9572	0.9815	0.9752	0.9626	0.9818	0.9599	0.9878	**0.9976**
seq3	0.9878	0.9701	0.9819	0.9846	0.9585	0.9919	0.9989	0.9998	**0.9999**
seq4	0.9945	0.9801	0.9925	0.9966	0.9633	0.9972	0.9875	0.9615	**0.9998**
seq5	0.9843	0.9979	0.9814	0.9897	0.9208	0.9915	0.9891	0.9429	**0.9996**
seq6	0.9871	0.9933	0.5678	0.9945	0.7681	0.9512	0.8537	0.9881	**0.9998**

TABLE V
THE VALUES OF SCRG AND BSF OBTAINED THROUGH USING DIFFERENT VALUE OF β.

| Sequence	$\beta.=98$		$\beta.=95$		$\beta.=90$		$\beta.=85$		$\beta.=75$		$\beta.=65$	
	BSF	SCRG	BSF	SCRG	BSF	SCRG	BSF	SCRG	BSF	SCRG	BSF	SCRG
seq1	2.631	3.676	4.234	13.233	12.427	23.471	6.366	16.471	1.401	3.839	0.532	2.890
seq2	5.429	7.083	7.026	18.631	5.572	4.049	2.548	1.275	2.259	1.125	2.059	1.037
seq3	7.939	6.041	6.621	3.762	7.914	6.014	8.736	15.367	5.268	2.473	1.563	1.371
seq4	3.265	6.598	5.596	10.763	10.325	14.286	6.482	16.291	2.514	4.865	2.123	2.563
seq5	1.241	9.542	6.417	10.596	9.524	17.634	3.258	2.537	2.014	1.897	1.009	1.569
seq6	5.653	11.253	8.634	18.210	3.278	6.261	2.479	3.569	1.230	3.541	1.084	3.294
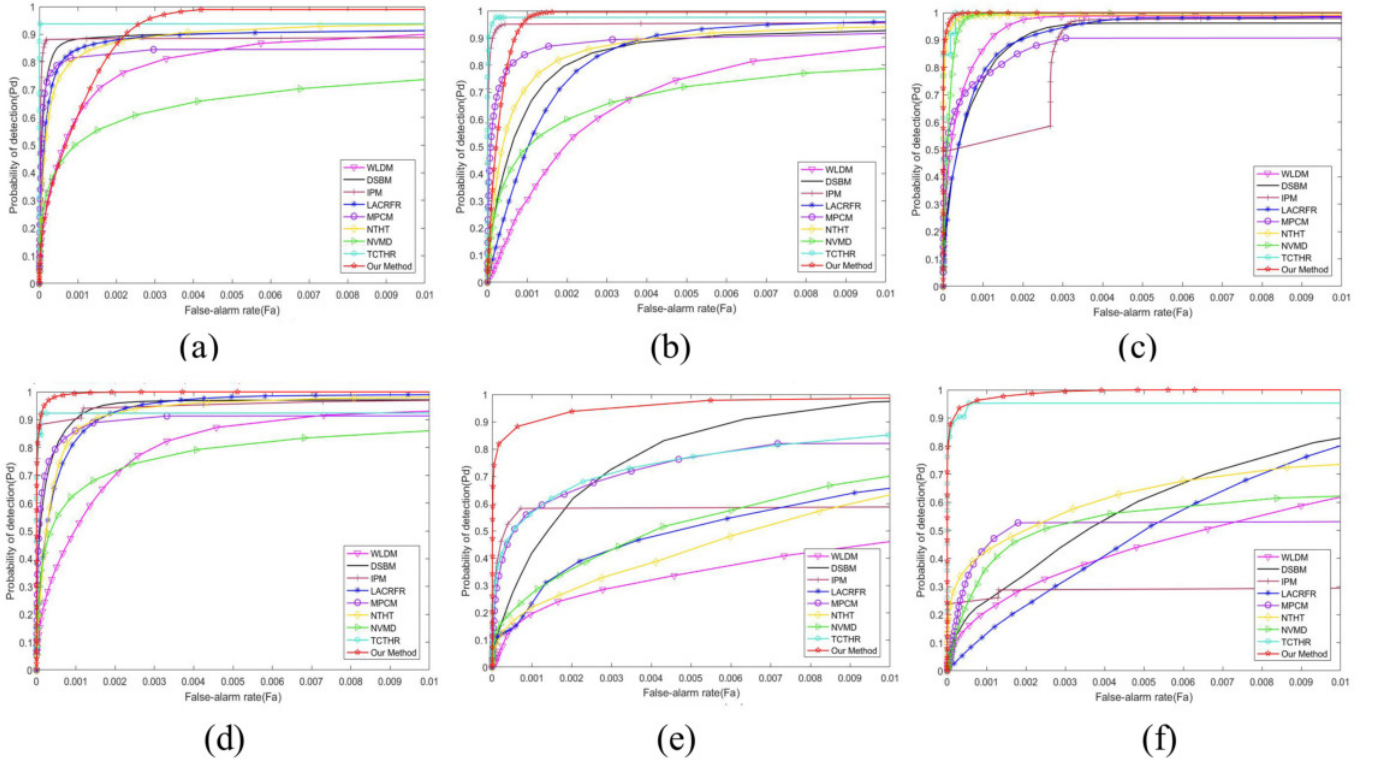
Fig. 9. ROC curves of nine methods for the six sequences. (a) seq1. (b) seq2. (c) seq3. (d) seq4. (e) seq5. (f) seq6.

TABLE VI
THE DETECTION RESULTS THROUGH DIFFERENT TOP-HAT ELEMENTS.

Sequence	Classical top − hat		Weighted ring top − hat	
	Pd	Fa	Pd	Fa
seq1	0.461	0.540	**0.877**	**0.123**
seq2	0.406	0.594	**0.808**	**0.192**
seq3	0.957	0.043	**0.981**	**0.019**
seq4	0.701	0.299	**0.981**	**0.019**
seq5	0.029	0.971	**0.913**	**0.087**
seq6	0.733	0.267	**0.762**	**0.238**

E. Parameter analysis

In this paper, the parameter β is the coefficient of the morphological regularization term in the objective function we need to optimize. It represents the influence of the morphological top hat transformation we use on the detection effect of our algorithm. If β is large, the morphological operation would have a larger weight for our detection, and vice versa, the weight is smaller. Therefore, to achieve a better target detection effect, we set different β values and conduct comparative experiments if the values of β are taken as β=98, 95, 90, 85, 75 and 65. We have listed the specific indicators in Table V.

Here, we can clearly see the values of BSF and SCRG when using different β values for different sequences. For sequence 1, sequence 4 and sequence 5, when the β value is 90, the values of BSF and SCRG tend to be the maximum, for sequence 2 and sequence 6, when the β value is 95, the values of BSF and SCRG tend to be the maximum, for Sequence 3, the corresponding β value is 85.In the above we mentioned that the larger the BSF, the better the background suppression effect, and the larger the SCRG, the better the enhancement effect of small targets.Therefore, for the overall effect of the algorithm, we set the parameter β to 90.
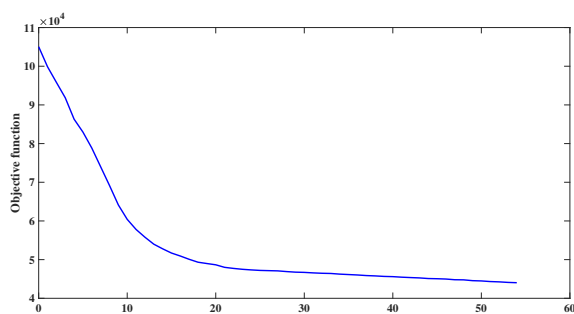

Fig. 10. The convergence analysis of our proposed algorithm.

F. Complexity and Convergence Analysis

The computational complexity and Convergence in our experimental environment are discussed in this section. According to the optimization, the solution of the target and the solution of the double nuclear norm constitute the majority of the computational complexity of the model.

We define the size of the images as $X \times Y$, and x and y are the rows and columns of the mode-3 unfolding. The ring structural element determines the solution of the target. The structure element solution is computed in $O(X \times Y)$, and the dilation operation and erosion operation are both computed in $O(X \times Y)$. Therefore, the computational complexity of the target solution is $O(X \times Y)$. The complexity of the double nuclear norm solution is composed mainly of SVD decomposition with a complexity of $O(x \times y)$. Considering that there are n iterations in the process of small target detection, the computational complexity of our model is approximately $O(n \times x \times y)$. All the experiments in this paper are conducted on a laptop computer with an Intel Core i5-6300 CPU and 12 GB RAM using MATLAB R2016a. Taking sequence 3 as an example, approximately 2.77 s are required for a frame picture to realize infrared small target detection. Furthermore, the convergence analysis is shown in Fig. 10, after many iterations, the value of the objective function tends to be stable, indicating that our method can finally find an optimal solution. Moreover, the number of iterations of the objective function approaching the optimal value is not very large, which proves that our model can easily achieve the convergence .

VI. CONCLUSION

In this paper, a model based on the double nuclear norm and ring weighted structural elements is proposed to solve the infrared small target detection problem. The model combines the characteristics of the low-rank tensor and prior knowledge of structural elements and achieves great performance in infrared small target detection. Experiments show that the model can maintain a low false alarm rate and high accuracy for different targets in different backgrounds, and it can improve the background suppression and target enhancement.

REFERENCES

[1] C. L. P. Chen, H. Li, Y. Wei, T. Xia, Y. Tang, "A local contrast method for small infrared target detection," IEEE Transactions on Geoscience and Remote Sensing, vol. 52, no. 1, pp. 574-581, 2014.

[2] X. K. Wang, Laurence. T. Yang, H. G. Li, M. Lin, J.J. Han, Bernady. O. Apduhan, "NQA: A Nested Anti-collision Algorithm for RFID Systems", ACM Transactions on Embedded Computing Systems, vol. 18, no. 4, 2019.

[3] M. Malanowski, K. Kulpa, "Detection of Moving Targets With Continuous-Wave Noise Radar: Theory and Measurements," in IEEE Transactions on Geoscience and Remote Sensing, vol. 50, no. 9, pp. 3502-3509, 2012.

[4] S. Kim, J. Lee, "Scale invariant small target detection by optimizing signal-to-clutter ratio in heterogeneous background for infrared search and track," Pattern Recognition, vol. 45, no. 1, pp 393-406, 2012.

[5] M. Zeng, J. Li, P. Zhang, "The design of top-hat morphological filter and application to infrared target detection," Infrared Physics and Technology, vol. 48, pp, 67-76, 2006.

[6] J. Liu, P. Musialski, P. Wonka, J. Ye , "Tensor completion for estimating missing values in visual data," IEEE International Conference on Computer Vision. vol. 35, pp 208-220, 2013.

[7] H. N. Phien, H. D. Tuan, J. A. Bengua, M. N. Do, "Efficient tensor completion: Low-rank tensor train,"arXiv preprint arXiv:1601.01083, 2006.

[8] Y. Dai, Y. Wu, "Reweighted infrared patch-tensor model with both nonlocal and local priors for single-frame small target detection," IEEE Journal of Selected Topics in Applied Earth Observations and Remote Sensing, vol. 10, no. 8, pp. 3752-3767, 2017.

[9] Y. He, M. Li, J. Zhang, and Q. An, "Small infrared target detection based on low-rank and sparse representation," Infrared Physics and Technology, vol.68, pp.98-109, 2015.

[10] I. S. Reed, R. M. Gagliardi, and L. B. Stotts, "Optical moving target detection with 3D matched filtering," IEEE Trans. Aerosp. Electron. Syst., vol. 24, no. 4, pp. 327–336, 1988.

[11] S. D. Deshpande, M. H. Er, R. Venkateswarlu, P. Chan, "Max-mean and max-median filters for detection of small targets," International Society for Optics and Photonics. vol. 3809, pp. 74–83, 1999.

[12] M. Li, T. Zhang, W. Yang, and X. Sun, "Moving weak point target detection and estimation with three-dimensional double directional filter in IR cluttered background," Opt. Eng., vol. 44, pp. 107007-1–107007-4, Oct. 2005.

[13] K. Melendez and J. Modestino, "Spatiotemporal multiscan adaptive matched filtering," International Society for Optics and Photonics, vol. 2561, pp. 51–65, Sep. 1995.

[14] H. Deng, X. Sun, M. Liu, C. Ye, X. Zhou, "Small Infrared Target Detection Based on Weighted Local Difference Measure," IEEE Transactions on Geoscience and Remote Sensing, vol. 54, no. 7, pp. 4204-4214, 2016.

[15] Y. Wei, X. You, H. Li, "Multiscale patch-based contrast measure for small infrared target detection," Pattern Recognition, vol. 58, pp. 216-226, 2016.

[16] P. Chiranjeevi, S. Sengupta, "Detection of Moving Objects Using Multichannel Kernel Fuzzy Correlogram Based Background Subtraction," in IEEE Transactions on Cybernetics, vol. 44, no. 6, pp. 870-881, 2014.

[17] H. Deng, X. Sun, X. Zhou, "A Multiscale Fuzzy Metric for Detecting Small Infrared Targets Against Chaotic Cloudy/Sea-Sky Backgrounds," IEEE Transactions on Cybernetics, vol. 49, no. 5, pp. 1694-1707, 2019.

[18] G. Matheron, "Random Sets and Integral Geometry, Willey," New York, 1975.

[19] J. Serra, "Image analysis using mathematical morphology," IEEE transactions on pattern analysis and machine intelligence, no. 4, pp. 532–550,1982.

[20] A. A Nayak, P. S Venugopala, H Sarojadevi, "An Approach to Improvise Canny Edge Detection using Morphological Filters," International Journal of Computer Applications, vol. 116, no. 9, pp. 38 – 42, Apr. 2015.

[21] J. Almotiri, K. Elleithy and A. Elleithy, "A Multi-Anatomical Retinal Structure Segmentation System for Automatic Eye Screening Using Morphological Adaptive Fuzzy Thresholding," IEEE Journal of Translational Engineering in Health and Medicine, vol. 6, 2018.

[22] A. Serna and B. Marcotegui, "Detection, segmentation and classification of 3D urban objects using mathematical morphology and supervised learning." ISPRS Journal of Photogrammetry and Remote Sensing, vol. 93, pp. 243-255, jul. 2014.

[23] F. Zhang, C. Li and L. Shi, "Detecting and tracking dim moving point target in IR image sequences," Infrared Physics and Technology, vol. 46, pp. 323-328, 2005.

[24] R. Kushol, M. H. Kabir, M. S. Salekin and A. B. M. A. Rahman, "Contrast Enhancement by Top-Hat and Bottom-Hat Transform with Optimal Structuring Element: Application to Retinal Vessel Segmentation," Image Analysis and Recognition: 14th International Conference, ICIAR 2017 Springer, Cham, 2017.

[25] S. Roychowdhury, D. Koozekanani and K. K. Parhi, "Iterative Vessel Segmentation of Fundus Images," IEEE Transactions on Biomedical Engineering, vol. 62, no. 7, pp. 1738-1749, 2015.

[26] X. Bai, F. Zhou and B. Xue, "Image enhancement using multi scale image features extracted by top-hat transform," Optics and Laser Technology, vol. 44, no. 2, pp. 328-336, 2012.

[27] M. Liao, Y. Zhao, X. Wang and P. Dai, "Retinal vessel enhancement based on multi-scale top-hat transformation and histogram fitting stretching," Optics and Laser Technology, vol. 58, pp. 56-62, 2014.

[28] Y. Bin and P. Xiong, "Small target detection method on morphological top-hat operator," Image Graphics, pp. 1006-8961, 2002.

[29] H. Zhu, J. Zhang, G. Xu and L. Deng, "Balanced Ring Top-Hat Transformation for Infrared Small-Target Detection With Guided Filter Kernel," in IEEE Transactions on Aerospace and Electronic Systems, vol. 56, no. 5, pp. 3892-3903, Oct. 2020.

[30] L. Deng, J. Zhang, G.Xu and H.Zhu "Infrared Small Target Detection via Adaptive M-Estimator Ring Top-Hat Transformation," Pattern Recognition, vol. 107729, Nov. 2020.

[31] X. Bai, F. Zhou, T. Jin and Y. Xie, "Infrared Small Target Detection and Tracking under the Conditions of Dim Target Intensity and Clutter Background," International Society for Optics and Photonics, vol. 6786, pp. 678-699, Nov. 2007.

[32] X. Bai, Xiangzhi, Y. Xie and T. Jin, "Adaptive Morphological Method for Clutter Elimination to Enhance and 36Detect Infrared Small Target,"IEEE Geoscience and Remote Sensing Letters, vol. 0, pp. 47–52, Jan. 2008.

[33] Y. Chen and Y. Xin . "An Efficient Infrared Small Target Detection Method Based on Visual Contrast Mechanism," IEEE Geoscience and Remote Sensing Letters, vol. 13, no. 7, pp. 962-966, 2016.

[34] H. Zhu, H. Ni, S. Liu, G. Xu and L. Deng, "TNLRS: Target-Aware Non-Local Low-Rank Modeling With Saliency Filtering Regularization for Infrared Small Target Detection," IEEE Transactions on Image Processing, vol. 29, pp. 9546-9558, 2020.

[35] X. Bai, F. Zhou, and Y . Xie, "New class of top-hat transformation to enhance infrared small targets," International Society for Optics and Photonics, vol. 17, no. 3, 2008.

[36] X. Bai and F. Zhou, "Analysis of new top-hat transformation and the application for infrared dim small target detection," IEEE Geoscience and Remote Sensing Letters, vol. 43, no. 6, pp. 2145–2156, 2010.

[37] C. Gao, D. Meng, Y. Yang, Y. Wang, X. Zhou and A. G. Hauptmann, "Infrared Patch-Image Model for Small Target Detection in a Single Image," IEEE Transactions on Image Processing, vol. 22, no. 12, pp. 4996-5009, Dec. 2013.

[38] Y. Sun, J. Yang, Y. Long, Z. Shang and W. An, "Infrared Patch-tensor Model with Weighted Tensor Nuclear Norm for Small Target Detection in A Single Frame," IEEE Transactions on Image Processing, vol. 4, 2018.

[39] H. Zhang, J. Yang, F. Shang, C. Gong and Z. Zhang, "LRR for subspace segmentation via tractable schatten-p norm minimization and factorization," IEEE Transactions on Cybernetics, vol. 49, no. 5, pp. 172–1734, 2019.

[40] G. Lerman and T. Zhang, "Robust recovery of multiple subspaces by geometric lp- minimization," The Annals of Statistics, vol. 39, no. 5, pp. 2686–2715, 2011.

[41] S. Wang, D. Liu, and Z. Zhang, "Nonconvex relaxation approaches to robust matrix recovery," Twenty-Third International Joint Conference on Artificial Intelligence, 1764–1770, Aug, 2013.

[42] M. Malek-Mohammadi, M. Babaie-Zadeh, and M. Skoglund, "Performance guarantees for Schatten-p quasi-norm minimization in recovery of low-rank matrices," Signal. Process, vol. 114, pp. 225–230, Sep. 2015

[43] X. Piao, Y. Hu, J. Gao, Y. Sun and B. Yin, "Double Nuclear Norm Based Low Rank Representation on Grassmann Manifolds for Clustering," Proceedings of the IEEE Conference on Computer Vision and Pattern Recognition, pp. 12075-12084, 2019.

[44] Y. Li, Y. Zhang, J. Yu, Y. Tan, J. Tian, J. Ma, "A novel spatio-temporal saliency approach for robust dim moving target detection from airborne infrared image sequences," Information Sciences, vol. 10, no. 369, pp. 548-563, 2016.

[45] S. Qi, J. Ma, C. Tao, C. Yang and J. Tian, "A robust directional saliency-base method for infrared small-target detection under virious complex backgrounds," IEEE Geoscience and Remote Sensing Letters, vol. 10, no. 3, pp.495-499, 2013.

[46] X. Wang and Z. Peng. "Infrared Small Target Detection via Nonnegativity-Constrained Variational Mode Decomposition." IEEE Geoscience and Remote Sensing Letters, vol. 14, np. 10, pp. 1700-1704, 2017.

[47] H. Zhu, S. Liu, L. Deng, Y. Li and F. Xiao, "Infrared Small Target Detection via Low-Rank Tensor Completion With Top-Hat Regularization," IEEE Transactions on Geoscience and Remote Sensing, vol. 58, no. 2, pp. 1004-1016, 2019.

[48] E. Acar, D. M. Dunlavy, T. G. Kolda, and M. Mørup, "Scalable tensor factorizations for incomplete data," Chemometrics and Intelligent Laboratory Systems, vol. 106, no. 1, pp. 41–56,2011.

[49] P . Tichavsk' y, A.-H. Phan, and A. Cichocki, "Numerical cp decomposition of some difficult tensors," Journal of Computational and Applied Mathematics, vol. 317, pp. 362–370, 2017.

[50] Y .-F. Li, K. Shang, and Z.-H. Huang, "Low tucker rank tensor recovery via admm based on exact and inexact iteratively reweighted algorithms," Journal of Computational and Applied Mathematics, vol. 331, pp. 64–81, 2018.

[51] X. Li, M. K. Ng, G. Cong, Y . Ye, and Q. Wu, "MR-NTD: manifold regularization nonnegative tucker decomposition for tensor data dimension reduction and representation," IEEE transactions on neural networks and learning systems, vol. 28, no. 8, pp. 1787–1800, 2017.

[52] S. Gandy, B. Recht, and I. Yamada, "Tensor completion and low-n-rank tensor recovery via convex optimization," Chemometrics and Intelligent Laboratory Systems, vol. 27, no. 2, pp. 025010, 2011.

[53] K. Braman, "Third-order tensors as linear operators on a space of matrices," Linear Algebra and its Applications, vol. 433, no. 7, pp. 1241–1253, 2010.

[54] M. E. Kilmer and C. D. Martin, "Factorization strategies for third-order tensors," Linear Algebra and its Applications, vol.435, no. 3, pp. 641–658, 2011.

[55] T. X. Jiang, M. K. Ng, X. L. Zhao, "Framelet Representation of Tensor Nuclear Norm for Third-Order Tensor Completion," IEEE Transactions on Image Processing, vol. 29, no.1, pp. 7233-7244, 2020.

[56] J. Xue, Y. Zhao, W. Liao and J. C. -W. Chan, "Multi-Layer Sparsity-based Tensor Decomposition for Low-rank Tensor Completion," IEEE

Transactions on Neural Networks and Learning Systems, 2021, doi: 10.1109/TNNLS.2021.3083931.

[57] Y. Bu, "Hyperspectral and Multispectral Image Fusion via Graph Laplacian-Guided Coupled Tensor Decomposition," IEEE Transactions on Geoscience and Remote Sensing, vol. 59, no.1, pp. 648-662, 2021.

[58] J, Fan and L, Ding and YD, Chen and U, Madeleine, "Factor group-sparse regularization for efficient low-rank matrix recovery,"Advances in Neural Information Processing Systems, vol. 32, pp. 5104-5114, 2019.

[59] B, Wen. and Y , Li. and L , Pfister. and Y, Bresler, "Joint Adaptive Sparsity and Low-Rankness on the Fly: An Online Tensor Reconstruction Scheme for Video Denoising," IEEE International Conference on Computer Vision (ICCV), pp. 241-250, 2017.

Guoxia Xu received the B.S. degree in information and computer science from Yancheng Teachers University, Jiangsu Yancheng, China in 2015, and the M.S. degree in computer science and technology from Hohai University, Nanjing, China in 2018. He was a research assistant in City University of Hong Kong and Chinese University of Hong Kong. Now, he is pursing his Ph.D. degree in Department of Computer Science, Norwegian University of Science and Technology, Gjøvik Norway. His research interest includes pattern recognition, image processing, and computer vision. E-mail: gxxu.re@gmail.com

Lizhen Deng received the B.S. degree in electronic information science and technology from Huaibei Coal Industry Teachers College, Huaibei, China, in 2007, and the M.S. degree in communication and information systems from Nanjing University of Aeronautics and Astronautics, Nanjing, China, in 2010. She received her Ph.D. degree in electrical engineering from Huazhong University of Science and Technology, China, in 2014. In 2014, she joined the Nanjing University of Posts and Telecommunica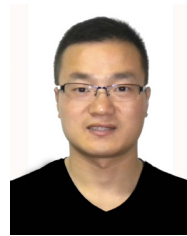tions, Nanjing, China. Her current research interests include image processing, computer vision, pattern recognition, and spectral data processing. E-mail: alicedenglzh@gmail.com

Dongyuan Xu received B.S. degree in communication engineering from Soochow University, SuZhou, China, in 2018. She is now pursuing her master degree in electronic and communication in Nanjing University of Posts and Telecommunications. Her current research interest is image processing. E-mail: xudy1996@163.com

Hu Zhu received the B.S. degree in mathematics and applied mathematics from Huaibei Coal Industry Teachers College, Huaibei, China, in 2007, and the M.S. and Ph.D. degrees in computational mathematics and pattern recognition and intelligent systems from Huazhong University of Science and Technology, Wuhan, China, in 2009 and 2013, respectively. In 2013, he joined the Nanjing University of Posts and Telecommunications, Nanjing, China. His research interests include pattern recognition, image processing, and computer vision. E-mail: peter.hu.zhu@gmail.com